

## Dynamics of chemically powered nanodimer motors subject to an external force

Yu-Guo Tao<sup>a)</sup> and Raymond Kapral<sup>b)</sup>

*Department of Chemistry, Chemical Physics Theory Group, University of Toronto, Ontario M5S 3H6, Canada*

(Received 7 May 2009; accepted 18 June 2009; published online 13 July 2009)

The chemically powered self-propelled directed motions of nanodimer motors confined in a rectangular channel and subject to an applied external conservative force are investigated using hybrid molecular dynamics/multiparticle collision dynamics. The influence of factors, such as dimer sizes, chemical reaction type, and the nature of the interaction potentials between dimer monomers and solvent molecules, on the propulsion force and friction constant are examined. The stall force, for which the nanodimer has zero net velocity, and the thermodynamic efficiency of the motor are calculated. Both irreversible and reversible chemical reactions are considered. The simulation results are compared to theoretical predictions which are able to capture the major features of the self-propelled motion. © 2009 American Institute of Physics. [DOI: 10.1063/1.3174929]

### I. INTRODUCTION

Molecular motors are devices that use chemical energy to generate directed motion. Typically, they operate in a fluid environment in the low Reynolds number regime<sup>1,2</sup> and thermal noise plays an important role in their dynamics.<sup>3,4</sup> Biomolecular motors, such as kinesins, myosins, and dyneins, use the chemical free energy released by the hydrolysis of adenosine triphosphate (ATP) as their fuel in order to produce a mechanical force that results in linear motion.<sup>5-9</sup> ATPase is an example of a rotary motor that consumes ATP to generate an electrochemical gradient or uses an electrochemical gradient to produce ATP; this motor is part of the flagellar drive motor in some bacteria.<sup>10</sup> These motors can efficiently convert chemical energy into mechanical work and have important roles to play in transport and assembly processes in the cell. Most biological motors have fairly complex molecular structures that undergo conformational changes as a result of energy supplied by various chemical reactions that couple to the conformational dynamics. Extensive experimental and theoretical studies have been carried out to investigate the essential features of the reactions and conformational dynamics that underlie the operations of specific biological motors.<sup>5-18</sup>

The design of synthetic molecular motors that can effect active transport processes is a research effort in nanotechnology that can lead to new applications.<sup>19</sup> Synthetic molecular motors, acting as rotors, switches, brakes, and ratchets, have been designed in a number of different forms and fabricated from numerous materials.<sup>19-23</sup> These motors, like their biological counterparts, depend either on conformational changes or on localized asymmetric catalytic reactions for their propulsion but have much simpler structures. Examples that exploit asymmetrical conformational changes for their motion are the artificial flagellar swimmer, whose tail is

composed of magnetic colloidal particles linked by DNA biopolymers,<sup>24,25</sup> and the one-dimensional swimmer model composed of linked beads that undergo nonreciprocal displacements.<sup>26,27</sup> The bimetallic nanorod motor, consisting of catalytic platinum and noncatalytic gold segments, exhibits self-propelled motion in an aqueous solution of hydrogen peroxide and has been extensively studied.<sup>28-37</sup> The directed motions of molecular motor models that rely on an asymmetric distribution of reaction products and phoretic mechanisms to generate forces have been studied analytically and experimentally.<sup>38-40</sup>

Here, we focus on the dynamics of a class of such synthetic molecular motors. In order to obtain a molecular description of chemically powered directed motion, a simple nanodimer model was constructed and investigated previously.<sup>41-43</sup> The dimer consisted of linked catalytic and noncatalytic spheres immersed in a solvent containing reactive  $A$  species. An irreversible reaction  $A + C \rightarrow B + C$  occurred at the catalytic end. The existence of a nonequilibrium gradient of  $B$  species in conjunction with different forces on the dimer ends provided the driving force on the nanodimer that resulted in directed motion. The nanodimer dynamics was simulated using a hybrid molecular dynamics/multiparticle collision dynamics scheme.<sup>44-46</sup> The simplicity and microscopic specification of the model allowed a theoretical analysis of the propulsion mechanism to be carried out. Here, we focus on the dynamics of such motors with an applied external force in order to mimic the behavior of molecular motors operating under a load.<sup>47</sup> The dimer is restricted to a narrow rectangular channel and a conservative external force is applied opposite to its directed motion. The stall force and thermodynamic efficiency of the nanodimer are computed, and the factors that determine these quantities are discussed.

In Sec. II the mesoscopic model for the nanodimer and solvent is described, and the technical aspects of the simulation method which arise because of the presence of an exter-

<sup>a)</sup>Electronic mail: ytao@chem.utoronto.ca.

<sup>b)</sup>Electronic mail: rkapral@chem.utoronto.ca.

nal force are discussed. Section III describes the particle-based theoretical model for the propulsion force from which the dimer velocity can be computed. Simulation results are presented for the average dimer velocity as a function of the external force for various system parameters. The friction coefficient is extracted from the simulation data and compared with theoretical predictions. In Sec. IV the thermodynamic efficiency of the nanodimer is computed for various interaction potentials between the noncatalytic monomer and the solvent  $B$  particles, and different chemical reaction parameters. The factors that determine the magnitude of the efficiency are discussed. Finally, the conclusions of our study are presented in Sec. V.

## II. NANODIMER MODEL AND DYNAMICS

The nanodimer consists of linked catalytic ( $C$ ) and noncatalytic ( $N$ ) spherical monomers with a fixed internuclear separation  $R$ ,<sup>41–43</sup> and is confined to a rectangular channel in order to suppress orientational Brownian motion. The parallel walls of the channel restrict the motion of the dimer in both the  $x$  and  $y$  directions through monomer-wall, 9-3-Lennard-Jones (LJ) interactions,

$$V_{\text{LJ}}^{93}(r) = \epsilon_w \left[ \left( \frac{\sigma_w}{r} \right)^9 - \left( \frac{\sigma_w}{r} \right)^3 \right]. \quad (1)$$

Here  $\epsilon_w$  and  $\sigma_w$  are the wall energy and distance parameters. We take  $\sigma_w = L_i/2$ , with  $L_i$  ( $i=x$  or  $y$ ) the wall separation along the  $x$  or  $y$  directions. A constant external force is applied to the center of mass of the dimer along the  $z$  direction in order to investigate its response to an external load.

The channel also contains  $A$  and  $B$  solvent molecules with identical masses,  $m$ . The masses of the catalytic and the noncatalytic spheres are adjusted according to their diameters,  $d_C$  and  $d_N$ , to ensure that the mass densities of the monomers are approximately the same as those of the solvent. The solvent  $A$  molecules interact with both dimer monomers through repulsive LJ potentials,

$$V_{\text{LJ}}^R(r) = 4\epsilon_A \left[ \left( \frac{\sigma_S}{r} \right)^{12} - \left( \frac{\sigma_S}{r} \right)^6 + \frac{1}{4} \right], \quad r \leq r_c, \quad (2)$$

with the cutoff distance  $r_c = 2^{1/6}\sigma_S$ , where  $S=C, N$ . The  $B$  molecules interact with the catalytic sphere through the same repulsive LJ potential, but interact with the noncatalytic sphere through either a repulsive LJ potential with a different energy parameter  $\epsilon_B$  or a truncated attractive LJ potential,

$$V_{\text{LJ}}^A(r) = 4\epsilon_B \left[ \left( \frac{\sigma_N}{r} \right)^{12} - \left( \frac{\sigma_N}{r} \right)^6 \right] s(r), \quad (3)$$

where the switching function  $s(r) = 1$  ( $r \leq r_t$ ) or  $s(r) = 1 - [(r - r_t)^2(3r_c - 2r - r_t)] / (r_c - r_t)^3$  ( $r_t < r \leq r_c$ ) smoothly truncates the potential to zero. We take  $r_t = 1.1688\sigma_N$  and  $r_c = 1.3636\sigma_N$ . The total potential energy of the system is

$$V(\mathbf{r}^{N_A}, \mathbf{r}^{N_B}) = \sum_{\alpha=A}^B \sum_{i=1}^{N_\alpha} [V_{C\alpha}(r_{i\alpha}) + V_{N\alpha}(r'_{i\alpha})], \quad (4)$$

where  $\mathbf{r}^{N_\alpha} = (\mathbf{r}_{1\alpha}, \mathbf{r}_{2\alpha}, \dots, \mathbf{r}_{N_\alpha\alpha})$  and  $\mathbf{r}_{i\alpha}$  is the vector distance to solvent molecule  $i$  of species  $\alpha$  and  $r_{i\alpha}$  its magnitude.

Here,  $r'_{i\alpha} = |\mathbf{r}_{i\alpha} - R\hat{\mathbf{z}}|$ . The LJ potential between the  $C$  sphere and a solvent molecule of species  $\alpha=A, B$  is  $V_{C\alpha}$ , with a similar notation for the  $N$  sphere. Solvent-solvent interactions are accounted for by multiparticle collision dynamics (MPC) discussed below.

The chemical reaction,  $A + C \rightleftharpoons B + C$ , occurs at the  $C$  sphere. In our simulation the reaction  $A \rightarrow B$  occurs with probability  $p_A = p_R$  whenever  $A$  encounters the catalytic sphere.<sup>48</sup> For the reverse reaction we choose  $p_B = 1 - p_R$  for the probability of conversion of  $B$  to  $A$  on encounter with  $C$ , although the forward and reverse probabilities could have been chosen independently. For our choice of reaction probabilities the equilibrium constant is  $K_{\text{eq}} = p_R / (1 - p_R)$  and the irreversible reaction corresponds to  $p_R = 1$ . The reaction probability  $p_R$  is introduced to account for the fact that because of steric or energetic factors encounters with the catalytic sphere need not lead to reaction. The reaction model is easily generalized to describe the reaction event deterministically. For example, reactions may be allowed to occur only if the kinetic energy along the line of centers joining the catalytic sphere and solvent chemical species exceeds a threshold value.<sup>49</sup>

The self-propulsion of the nanodimer is simulated by a hybrid particle-based mesoscopic molecular dynamics (MD)/MPC algorithm<sup>44,45</sup> which consists of streaming and collision steps. In the streaming step, the dynamics of both solvent and monomer particles are governed by Newton's equations of motion. In the collision steps, which occur at time intervals  $\tau$ , the pointlike solvent particles are sorted into cubic cells with lattice size  $a_0$ . Multiparticle collisions among the solvent molecules are performed independently in each cell, and the postcollision velocity of solvent particle  $i$  in cell  $\xi$  is given by  $\mathbf{v}'_i = \mathbf{V}_\xi + \hat{\omega}_\xi(\mathbf{v}_i - \mathbf{V}_\xi)$ , where  $\hat{\omega}_\xi$  is a rotation matrix and  $\mathbf{V}_\xi$  is the center-of-mass velocity of that cell. The dynamics is microcanonical, satisfies mass, momentum, and energy conservation, and also preserves phase space volumes. For reviews of this method with applications see Refs. 50 and 51.

At chemical equilibrium there is no net nanodimer directed motion and propulsion relies on the system being out of equilibrium. In order to maintain the system in a nonequilibrium steady state,  $B$  molecules are converted back to  $A$  when they diffuse far enough away from the catalytic sphere. We choose the conversion cutoff radius  $\sigma_{B \rightarrow A} = R + d_N$ . This mimics the fluxes of  $A$  and  $B$  molecules into and out of the system that drive it out of equilibrium. Under these conditions the directed motion of the nanodimer can proceed indefinitely.

Other simulation details are as follows: The internuclear separation between the catalytic and the noncatalytic spheres is fixed at  $R$  by a holonomic constraint.<sup>52</sup> The distance  $R$  is chosen to prevent discontinuous potential changes when chemical reaction occurs on the catalytic monomer. All quantities reported below are expressed in dimensionless LJ units based on energy  $\epsilon$ , mass  $m$  and distance  $\sigma$  parameters:  $r/\sigma \rightarrow r$ ,  $t(\epsilon/m\sigma^2)^{1/2} \rightarrow t$ , and  $k_B T/\epsilon \rightarrow T$ . The rotation angle for multiparticle collisions is fixed at  $\alpha = 90^\circ$ . The average number of solvent molecules per cell is  $\gamma \approx 10$  in all simulations. The MD time step, which is used to integrate Newton's equa-

tions of motion with the velocity Verlet algorithm, is  $\Delta t = 0.01$ , while the multiparticle collision time is  $\tau = 0.5$ . With these parameters the total energy of the system exhibits only small fluctuations about a constant value with no drift. The lattice size of an MPC cell is  $a_0 = 1$ , and the system temperature is fixed at  $T = 1/6$ . The LJ potential parameter is chosen to be  $\epsilon_A = 1.0$  in all simulations, while  $\epsilon_B$  varies from 0.1 to 5.0 in order to investigate changes to both the speed and direction of the nanodimer movement.

Since the mean free path  $\lambda \approx 0.2$  is small compared to the MPC cell size, random shifts are applied in each direction of the simulation box in order to restore the Galilean invariance.<sup>53,54</sup> Periodic boundary conditions are used along the  $z$  direction, while the solvent molecules experience bounce-back boundary conditions in both wall directions. The system is subdivided into  $L_z/a_0$  cells in  $z$  direction, which is parallel to the walls, but  $L_x/a_0 + 1$  and  $L_y/a_0 + 1$  cells in  $x$  and  $y$  directions to account for the random grid shifts. At the walls, some cells are not completely filled by particles. In such cases, extra virtual point particles whose velocities are drawn from a Maxwell–Boltzmann distribution with zero mean velocity and variance  $\sqrt{k_B T/m}$  are added to conserve the solvent particle number density. Moreover, due to the existence of the external force, a thermostat must be employed after each MD time step in order to maintain the system at a constant temperature. To apply the thermostat, the simulation box is subdivided into  $L_x \times L_y/a_0$  strips parallel to both walls. In each strip, the new velocity  $\mathbf{v}'_i$  of each solvent particle  $i$  in cell  $\xi$  is obtained by rescaling the velocity relative to the center-of-mass velocity of that cell,

$$\mathbf{v}'_i = \mathbf{V}_\xi + \sqrt{\frac{k_B T}{k_B T'}} (\mathbf{v}_i - \mathbf{V}_\xi), \quad (5)$$

where  $k_B T'$  is calculated from

$$\sum_{i=1}^N \frac{1}{2} m (\mathbf{v}_i - \mathbf{V}_\xi)^2 = (N - \tilde{N}) k_B T', \quad (6)$$

where  $N$  and  $\tilde{N}$  denote the number of particles and the number of cells which contain particles within the specified strip, respectively.<sup>51,55</sup>

The inhomogeneous nonequilibrium gradient of the  $B$  particle density field in the vicinity of the noncatalytic  $N$  sphere is a key factor in the mechanism giving rise to directed motion.<sup>41,42</sup> Figure 1 shows an instantaneous configuration of the  $B$  molecule density around the asymmetric nanodimer in the steady state regime. The system reaches its nonequilibrium steady state in  $2 \times 10^5$  time units, while the total length of a simulation is  $10^6$  time units. In this simulation the reaction probability is  $p_R = 0.5$  and the external force is  $F_{ex} = -4.0$ . The total solvent molecule density field is approximately uniform, while the gradient in the  $B$  molecule density field varies from high to low from the catalytic to noncatalytic ends of the dimer.

An important aspect of the mechanism of the dimer motion is the nature of the coupling to the solvent hydrodynamic fields. Since the hybrid MPC dynamics conserves momentum, hydrodynamic interactions are accounted for in the simulations. The fluid flow field induced by the directed mo-

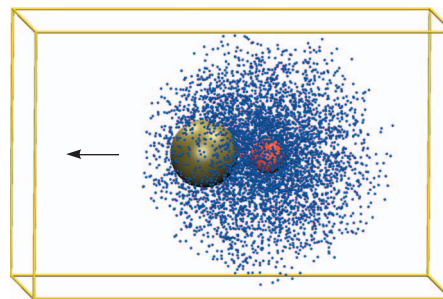


FIG. 1. Instantaneous configuration of  $B$  (dots) molecules in the vicinity of the nanodimer. The rectangular simulation box has dimensions  $32 \times 32 \times 50$  and contains 512 000 solvent molecules in total. The  $A$  molecules, which constitute the majority of the solvent particles, are not shown. The diameters of the catalytic (small) and the noncatalytic (large) spheres are  $d_C = 4.0$  and  $d_N = 8.0$ , respectively. Attractive LJ interactions between the solvent  $B$  molecules and the noncatalytic  $N$  sphere with an energy parameter  $\epsilon_B = 0.1$  are used. The arrow shows the direction along which a conservative external force is applied to the nanodimer center-of-mass. The self-propelled directed motion of the nanodimer is opposite to that of the applied force.

tion of the nanodimer depends significantly on the magnitude of the applied external force. Figure 2 plots the local solvent velocity field in the vicinity of the dimer in a  $2 \times 16 \times 20$  slice parallel to the nanodimer internuclear axis and the walls in the  $x$  direction. In Fig. 2(a) no external force is applied to the dimer. The nanodimer is propelled in the  $+z$  direction with the small catalytic sphere leading. The velocity of the dimer along the internuclear axis is  $V_z \approx 0.058$ . This directed motion is also evident in the solvent collective motions at the catalytic end where a fluid flow is generated in the same direction. The solvent “backflow” at the end of the larger noncatalytic sphere is also seen in this figure. In Fig. 2(b), we plot the solvent velocity flow field when a negative conservative

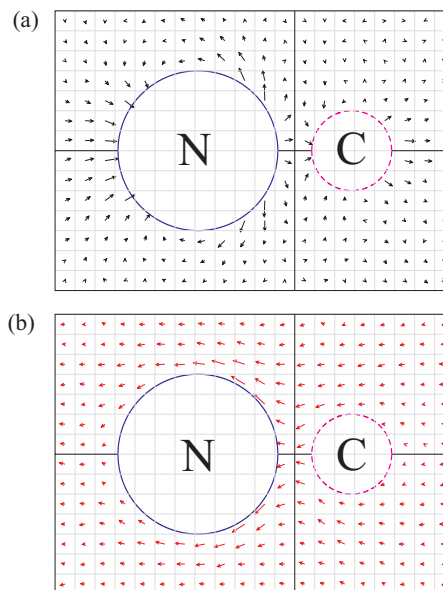


FIG. 2. The solvent molecule velocity field in the vicinity of the nanodimer. (a) No external force is applied. (b) The external force is  $F_{ex} = -7.0$ , for which the velocity of the nanodimer is nearly zero. In these simulations, the monomer diameters are  $d_C = 4.0$  and  $d_N = 8.0$ , and the wall separations are  $L_x = L_y = 32$ . The noncatalytic monomer interacts with  $B$  solvent particles through attractive LJ potentials with energy parameter  $\epsilon_B = 0.1$ .

force is applied on the nanodimer center of mass. The direction of the force is opposite to the dimer movement, while its magnitude  $F_{\text{ex}} = -7.0$  is close to the stall force  $F_0 = -6.8$  (see below) where directed dimer motion ceases. In this case the nearly stationary dimer imparts a momentum to the solvent that generates a flow field whose direction is opposite to the external-force-free motion, as if the dimer were swimming upstream.

### III. PROPULSION AND STALL FORCES

In the steady state regime, the sum of the external force and the propulsion force that is responsible for the directed motion of the dimer is balanced by the frictional force:

$$F_{\text{prop}} + F_{\text{ex}} + F_{\text{fric}} = 0. \quad (7)$$

The frictional force is  $F_{\text{fric}} = -\zeta V_z$ , where  $\zeta$  is the friction coefficient, and the propulsion force  $F_{\text{prop}} = \langle \hat{\mathbf{z}} \cdot \mathbf{F} \rangle$  is the steady state average of the force exerted on the fixed dimer by the solvent. As discussed earlier,<sup>41,42</sup> the propulsion force depends on the solvent-dimer forces and the nonequilibrium steady state  $A$  and  $B$  density fields:

$$\begin{aligned} \langle \hat{\mathbf{z}} \cdot \mathbf{F} \rangle = & - \sum_{\alpha=A}^B \int d\mathbf{r} \rho_{\alpha}(\mathbf{r}) (\hat{\mathbf{z}} \cdot \hat{\mathbf{r}}) \frac{dV_{C\alpha}(r)}{dr} \\ & - \sum_{\alpha=A}^B \int d\mathbf{r} \rho_{\alpha}(\mathbf{r}) (\hat{\mathbf{z}} \cdot \hat{\mathbf{r}}') \frac{dV_{N\alpha}(r')}{dr'}. \end{aligned} \quad (8)$$

Again,  $\mathbf{r}$  denotes coordinates measured with the catalytic  $C$  sphere as the origin, while  $\mathbf{r}'$  is defined with the noncatalytic  $N$  sphere as the origin and is related to  $\mathbf{r}$  by  $\mathbf{r}' = \mathbf{r} - R\hat{\mathbf{z}}$ . The steady state density can be written in the form  $\rho_{\alpha}(\mathbf{r}) = n_{\alpha}(\mathbf{r}) e^{-\beta[V_{C\alpha}(r) + V_{N\alpha}(r')]}$  in order to account for the solvent structure within the interaction range of the monomer-solvent potentials. To obtain a simple explicit expression for the propulsion force, the local steady state density  $n_{\alpha}(\mathbf{r})$  may be approximated by the solution of the diffusion equation in the absence of the noncatalytic sphere.<sup>42</sup> Using the result of such a calculation for a reversible reaction in Eq. (8), we find

$$\begin{aligned} \langle \hat{\mathbf{z}} \cdot \mathbf{F} \rangle = & -k_B T R_0 n_A^0 \frac{k_{f0}}{k_{f0} + k_{r0} + k_D} \int d\mathbf{r}' \frac{\hat{\mathbf{z}} \cdot \hat{\mathbf{r}}'}{|\mathbf{r}' + R\hat{\mathbf{z}}|} \\ & \times \frac{d}{dr'} [e^{-\beta V_{NA}(r')} - e^{-\beta V_{NB}(r')}] . \end{aligned} \quad (9)$$

Here,  $k_{f0}$  and  $k_{r0}$  are the forward and reverse reaction rate constants which characterize the reactive events that occur within a diffusive boundary layer around the catalytic sphere. For the purposes of obtaining a velocity estimate they can be approximated by a simple hard sphere collision model,  $k_{f0} = p_R Z_C$  and  $k_{r0} = (1 - p_R) Z_C$ , where the collision frequency is  $Z_C = \sigma_C^2 \sqrt{8\pi k_B T} / m$ . The Smoluchowski diffusion-controlled rate constant is  $k_D = 4\pi R_0 D$ , with  $D$  the common diffusion coefficient of the  $A$  and  $B$  molecules.<sup>49</sup> The reaction distance  $R_0$  is chosen to be  $R_0 = 2^{1/6} \sigma_C$ . Since the diffusion coefficient can be computed analytically for MPC dynamics<sup>50,51</sup> all quantities needed determine the propulsion force from this equation are known.

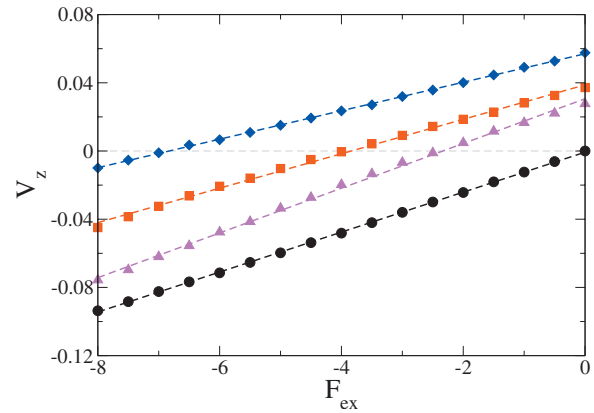


FIG. 3. The average velocity of the nanodimer  $V_z$  as a function of the applied external force  $F_{\text{ex}}$ . The monomer sizes are  $d_C = 4.0$  and  $d_N = 8.0$  in these simulations. For each value of the applied external force, the self-propulsion velocity of the nanodimer along its internuclear axis was determined from an average over ten independent realizations. Circles denote results where no chemical reaction occurs at the catalytic monomer; thus, the simulation box contains only  $A$  solvent molecules. Triangles and diamonds denote results where the interactions between the noncatalytic  $N$  sphere and  $B$  solvent particles are through either repulsive or attractive LJ potentials, respectively. In these two cases, the reaction probability is  $p_R = 1.0$  and the reaction is irreversible. The squares denote results for reversible reactions with  $p_R = 0.5$  for attractive interactions between the  $N$  sphere and  $B$  particles. All simulations were carried out in rectangular boxes with wall separations of  $L_x = L_y = 32$ .

From Eq. (7) and the expression for the frictional force we have

$$V_z = \frac{1}{\zeta} F_{\text{prop}} + \frac{1}{\zeta} F_{\text{ex}}. \quad (10)$$

The simulation data in Fig. 3 confirms the linear relationship between the average nanodimer velocity  $V_z$  and the applied external force  $F_{\text{ex}}$  for various system parameters. In this figure we show how the interaction potentials (attractive or repulsive), the wall separation, as well as the types of chemical reactions (irreversible or reversible or no reaction) influence the slopes in these plots that determine the friction coefficient, and the intercepts at zero external force that determine the propulsion force.

In the absence of chemical reaction, the propulsion force is zero as expected and the measured friction constant is  $\zeta = 85.4$ . This can be compared to a theoretical estimate based on the Oseen approximation,<sup>42</sup>

$$\zeta = \frac{\zeta_C + \zeta_N - 4\zeta_C \zeta_N \phi(R)}{1 - 2\zeta_C \zeta_N \phi^2(R)}, \quad (11)$$

where  $\phi = 1/(8\pi\eta R)$ . Here  $\zeta_C$  and  $\zeta_N$  are the friction coefficients of the catalytic and noncatalytic spheres. These friction coefficients can be decomposed approximately into microscopic and hydrodynamic contributions,  $\zeta_S^{-1} = \zeta_m^{-1} + \zeta_h^{-1}$  where

$$\zeta_m = \frac{8}{3} n \sigma_S^2 \sqrt{2\pi m k_B T}, \quad \zeta_h = 4\pi\eta\sigma_S, \quad (12)$$

where  $n$  is the number density of the solvent molecules and  $\eta$  is the viscosity of the solvent. Since the viscosity is known analytically for the MPC solvent,<sup>50,51,56,57</sup> the dimer friction

TABLE I. Average velocities of the center of mass of the nanodimer along its internuclear axis for an irreversible reaction. The applied constant external force varies from  $F_{\text{ex}}=-1.0$  to  $-9.0$ . The diameters of the  $C$  and  $N$  spheres are  $d_C=4.0$  and  $d_N=8.0$ , respectively. The internuclear separation is  $R=7.7$ . There are attractive interactions between  $N$  sphere and  $B$  molecules with  $\epsilon_B=0.1$ . The theoretical values are determined from Eq. (9) and the theoretical estimate for the friction in Eq. (11), while the hybrid results are calculated using the friction coefficient determined from simulations instead of the Oseen approximation. The lower portion of the table presents the results for a reversible reaction with  $p_R=0.5$  with external forces ranging from  $F_{\text{ex}}=-1.0$  to  $-4.0$ . Other parameters are the same as those in the top and middle parts of the table.

$F_{\text{ex}}$	0.0	-1.0	-2.0	-3.0	-4.0
Simulation	0.058	0.049	0.040	0.032	0.024
Theory	0.132	0.116	0.101	0.085	0.070
Hybrid	0.071	0.062	0.054	0.046	0.037
$F_{\text{ex}}$	-5.0	-6.0	-7.0	-8.0	-9.0
Simulation	0.015	0.007	-0.001	-0.010	-0.027
Theory	0.054	0.039	0.023	0.008	-0.023
Hybrid	0.029	0.021	0.012	0.004	-0.013
$F_{\text{ex}}$	0.0	-1.0	-2.0	-3.0	-4.0
Simulation	0.037	0.028	0.019	0.009	-0.001
Theory	0.066	0.050	0.035	0.019	0.004
Hybrid	0.040	0.030	0.021	0.012	0.002

can be estimated from this formula. This formula yields  $\zeta=64.4$ . Since the system initially contains only  $A$  solvent molecules and no reaction takes place, this is the friction coefficient for a pure  $A$  molecule solvent.

When reactions take place self-propulsion is achieved as indicated by the nonzero intercepts in Fig. 3. In addition the slopes of the lines change reflecting changes to the friction coefficient. In particular,  $\zeta=119.8$  for attractive LJ interactions and  $p_R=1$  (irreversible reaction),  $\zeta=76.3$  for repulsive LJ interactions and  $p_R=1$ , and  $\zeta=106.9$  for attractive LJ interactions and  $p_R=0.5$ . The presence of  $B$  molecules in the solution as a result of reaction is responsible for the observed changes in the friction coefficients.

The value of the friction coefficient also depends strongly on the system dimension. Simulations of nanodimers with the same monomer sizes as above were carried out in two other rectangular boxes with wall separations of  $L_x=L_y=16$  and  $50$ , respectively. In the box with a narrower channel the distance from the central line of the box to the wall is  $8$ , which is about half of the  $B$  conversion cutoff radius  $\sigma_{B \rightarrow A}=15.7$ . The diffusion of  $B$  solvent molecules is affected by bounce-back collisions with the hard walls. Consequently, the  $B$  solvent density field in the vicinity of the noncatalytic sphere is different from that in boxes with larger wall separations. This results in a friction coefficient that is twice as large as that in the box with the wider channel. For  $L_x=L_y=50$  the friction constant is approximately equal to that for  $L_x=L_y=32$ , since the wall separation is large compared to the conversion cutoff distance. In this case only  $A$  molecules experience bounce-back collisions at the hard walls, and this has no effect on the solvent density gradient or the propulsion velocity of the nanodimer.

As can be seen from Eq. (10) the nanodimer velocity depends on the force and friction coefficient. Table I compares the simulated average velocities of the nanodimer for various values of the external force with theoretical predictions using Eq. (9). If theoretical estimates of the friction

tensor are used in this equation (results labeled “theory” in Table I), the magnitudes and trends in the nanodimer velocity are captured by this approximation but the predicted  $V_z$  values are not quantitatively accurate. To assess the role that the value of the friction coefficient plays in this prediction, we also present “hybrid” predicted values of  $V_z$  using Eq. (9) along with the measured friction coefficient. Other factors in the propulsion force expression remain the same. The purely theoretical value of  $V_z$  is approximately twice that of the simulation value, however, the hybrid estimate differs by only 20%. The remaining discrepancy may be attributed to the approximate form of the nonequilibrium solvent density field which neglects of the presence of the noncatalytic sphere.

### A. Stall force

The stall force  $F_0$  is the external force which must be applied to make the velocity of the motor zero. Since  $F_0=-F_{\text{prop}}$  the stall force varies with changes in various quantities such as the interaction potentials between monomers and solvent molecules, monomer sizes and nonequilibrium density fields. Figure 4(a) shows the effect of changes in the potential parameter  $\epsilon_B$  on the stall force. When  $\epsilon_B < \epsilon_A$ , the self-propelled motion of the dimer is in the direction of the  $C$  sphere and its average velocity  $V_z$  is positive. A negative external force must therefore be applied to stop the movement of the dimer. The stall force drops rapidly as  $\epsilon_B$  approaches  $\epsilon_A$ . For  $\epsilon_B = \epsilon_A$ , the reaction is simply a relabeling of chemical species: no propulsion force is generated and the nanodimer has a net velocity of zero. The stall force decreases much more slowly when  $\epsilon_B$  is larger than  $\epsilon_A$ . In this regime the nanodimer moves in the opposite direction and the stall force is positive.

Figure 4(b) shows how the stall force changes when the  $C$  sphere diameter varies from  $d_C=2.0$  to  $8.0$  with the  $N$  sphere diameter fixed at  $d_N=8.0$ . When  $d_C \leq 4.0$ , the size of

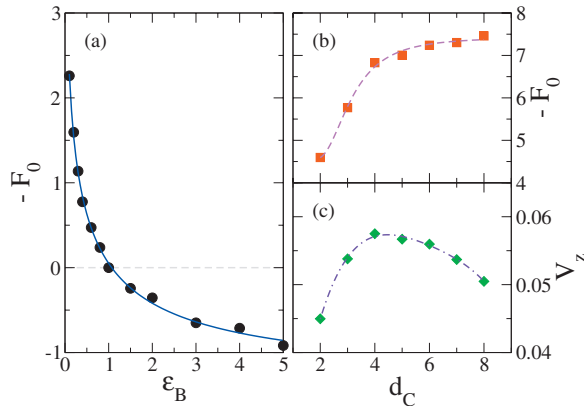


FIG. 4. The stall force as a function of (a) the energy parameter  $\epsilon_B$  and (b) the  $C$  sphere diameter  $d_C$ . The interaction potentials between the  $N$  sphere and  $B$  particles are repulsive and attractive in panels (a) and (b), respectively. Panel (c) plots  $V_z$  as a function of the  $C$  sphere diameter in the absence of an external force. The reaction probability in both cases is  $p_R = 1.0$ . The sphere diameters are  $d_C = 4.0$  and  $d_N = 8.0$  in (a). The  $N$  sphere diameter is fixed at  $d_N = 8.0$  in (b) and (c), while the potential parameter  $\epsilon_B = 0.1$ .

the  $C$  sphere does not have a strong effect on the value of the friction coefficient. In these cases, the dependence of  $F_0$  on  $d_C$  is similar to that of  $V_z$  on  $d_C$  in the absence of an external force, as shown in panel (c). As  $d_C$  increases, the maximum in  $V_z$  occurs at an intermediate size of the  $C$  sphere. Increasing  $d_C$  increases the chemical reaction rate but, at the same time, increases the internuclear separation between the two monomers. The increase in the reaction rate leads to a larger nonequilibrium  $B$  molecule gradient giving rise to a larger driving force on the nanodimer. An increase in the dimer bond length tends to reduce the propulsion force on the nanodimer since the  $N$  sphere is farther from the source of  $B$  molecules. The stall force is the negative of the propulsion force which is itself the product of  $V_z$  in the absence of an external force and the friction constant. As  $d_C$  increases, the friction constant  $\zeta$  also increases. Thus, the balance between these two competing factors is likely responsible for the plateau in  $F_0$  with increasing  $d_C$ .

#### IV. EFFICIENCY

Chemically powered molecular motors convert chemical free energy into mechanical work, driving the self-propelled directed movement. The thermodynamic efficiency of the power transduction of the motor is defined as the ratio between the power associated with the work done by the motor against an external conservative force and the power input due to chemical reaction.<sup>58,59</sup> For a reversible chemical reaction  $A + C \rightleftharpoons B + C$ , the thermodynamic efficiency can be computed from

$$\eta_{\text{TD}} = -\frac{V_z F_{\text{ex}}}{\Delta\mu\mathcal{R}}, \quad (13)$$

where  $\mathcal{R}$  is the net chemical reaction rate, and  $\Delta\mu$  is the change in the chemical potential in the reaction. For our system

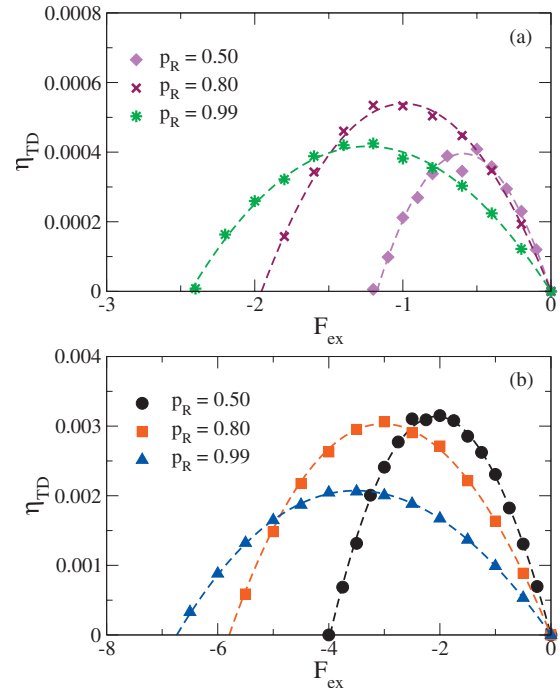


FIG. 5. Thermodynamic efficiency of the nanodimer as a function of the applied external force. Curves are fits using Eq. (15). In (a), the interaction forces between the  $N$  monomer and  $B$  particles are through repulsive LJ potentials, while in (b) they are attractive. The energy parameter is  $\epsilon_B = 0.1$  in both cases. The reaction probability of the reversible reaction  $A + C \rightleftharpoons B + C$  varies from  $p_R = 0.5$  to  $0.99$ . The diameters of the  $C$  and  $N$  monomers are  $d_C = 4.0$  and  $d_N = 8.0$ , respectively. Each value of the thermodynamic efficiency is the result of an average over ten independent realizations.

$$\Delta\mu = \mu_B - \mu_A = -k_B T \ln \frac{n_B n_A^{\text{eq}}}{n_B^{\text{eq}} n_A}. \quad (14)$$

Here  $n_A^{\text{eq}}$  and  $n_B^{\text{eq}}$  denote the equilibrium number densities of  $A$  and  $B$  species, respectively, while the steady state densities are again  $n_A$  and  $n_B$ . The net chemical reaction rate  $\mathcal{R}$  was calculated by counting the number of  $A \rightarrow B$  and  $B \rightarrow A$  reactive events at the catalytic sphere as a function of time and subtracting the corresponding rates to obtain the net rate. Substituting expression (10) for the average velocity in terms of the propulsion and external forces into Eq. (13), the thermodynamic efficiency can be rewritten as

$$\eta_{\text{TD}} = -\frac{F_{\text{ex}}^2 + F_{\text{prop}} F_{\text{ex}}}{\zeta \Delta\mu \mathcal{R}}. \quad (15)$$

The efficiency has its maximum when  $d\eta_{\text{TD}}/dF_{\text{ex}} = 0$ , which yields

$$\eta_{\text{max}} = \frac{F_{\text{prop}}^2}{4\zeta \Delta\mu \mathcal{R}} \quad (16)$$

and  $F_{\text{ex}} = -F_{\text{prop}}/2$ .

We compare the thermodynamic efficiencies in Fig. 5 for six nanodimer systems where the interactions are through either attractive or repulsive LJ potentials. For a reaction probability of  $p_R = 0.5$ , the corresponding values of some key quantities are compared and listed in Table II. For attractive LJ potentials we showed above that the propulsion force on the nanodimer is large so that  $V_z$  is about 2.6 times higher

TABLE II. Comparison of various quantities for systems with either attractive or repulsive LJ potentials between the  $N$  sphere and  $B$  solvent particles. The simulations are for a system in a box with size  $32 \times 32 \times 50$ . The reaction probability is  $p_R=0.5$ . The monomer diameters are  $d_C=4.0$  and  $d_N=8.0$ , respectively. The internuclear separation is  $R=7.7$ .

Potential	$V_z$	$\zeta$	$F_0$	$n_B/n_A$
Attractive	0.037	106.9	-4.0	0.009
Repulsive	0.014	82.2	-1.2	0.011

Potential	$\mathcal{R}_{A \rightarrow B}$	$\mathcal{R}_{B \rightarrow A}$	$\mathcal{R}$	$\eta_{\max}$
Attractive	33.9	17.8	16.1	0.31%
Repulsive	33.1	18.9	14.2	0.04%

than that for systems with repulsive potentials. Thus, the power associated with the mechanical work of the motor is larger for attractive forces. Also, Table II shows the  $A \rightarrow B$  and  $B \rightarrow A$  reaction rates for both attractive and repulsive potentials that contribute to the net rate  $\mathcal{R}$ , which is greater for attractive forces than for repulsive forces. However, the ratio of steady state densities  $n_B/n_A$  compensates for this factor and the net efficiency is larger for motors with attractive forces. The maximum of  $\eta_{TD}$  can vary by a factor of 8 by adjusting the interaction potentials between the dimer spheres and solvent molecules.

We have also investigated the influence of the reaction probability on the efficiency of the nanomotor. Increasing the reaction probability increases the propulsion force on the dimer; however, it also increases the net reaction rate and thus the power associated with chemical reaction. Consequently, as a result of the competition between these two effects, nanodimers with smaller reaction probabilities have a larger thermodynamic efficiency in the regime of lower applied conservative forces. The maximum thermodynamic efficiency achieved in our simulation is about 0.31%, which is much smaller than that of most macroscopic motors or biomolecular machines.<sup>47,60,61</sup> It is larger than the estimates for nanorods.<sup>31</sup>

## V. CONCLUSION

Several features of the simulations presented above are worth summarizing. By applying an external force to the self-propelled nanodimer a number of features of the dynamics could be probed in some detail. The friction that the dimer experiences could be extracted from the data and compared to simple theoretical predictions. The friction coefficient depends on the chemical composition of the medium, solvent properties and forces from the walls that confine the dimer motion. In addition, the stall force and efficiency of the motor were computed and the factors that influence their magnitudes could be determined. In our hybrid MD/MPC dynamics the motion of the nanodimer is coupled to the solvent by intermolecular forces, and the solvent dynamics preserves all conservation laws so that fluid flow and hydrodynamic interactions, which play an important part in the self-propelled motion, are taken into account. Because the transport properties of the MPC solvent are known, a theoretical analysis of dimer properties can be carried out in details.

The differences in the interactions of the reactive species with the dimer ends and the nonequilibrium chemical gradients generated by reaction give rise to the directed motion. Since the manner in which these general controlling factors enter the model description is easily seen, chemically powered nanodimers with velocities that are not quickly randomized by thermal fluctuations can be designed.<sup>42</sup> In particular, varying of the size of the noncatalytic sphere and manipulations of the interactions of the solvent with this part of the motor can be used to tune the velocity. These factors can be employed in the design of other engineered or model chemically powered motors.

Research into synthetic molecular motors is still at an early stage of development. The design characteristics, mechanisms of operation, and potential applications of such motors are all active research topics. The analysis of the factors that determine the propulsion forces and efficiencies of simple chemically powered motors of the sort considered in this paper should provide useful input when designing nanoscale motors that successfully compete with fluctuations to achieve directed motion.

## ACKNOWLEDGMENTS

Research supported, in part, by a grant from the Natural Sciences and Engineering Research Council of Canada.

- J. Happel and H. Brenner, *Low Reynolds Number Hydrodynamics* (Nijhoff, Dordrecht, 1965).
- E. M. Purcell, *Am. J. Phys.* **45**, 3 (1977).
- R. D. Astumian, *Science* **276**, 917 (1997).
- R. D. Astumian and P. Hänggi, *Phys. Today* **55** (11), 33 (2002).
- N. J. Carter and R. A. Cross, *Nature (London)* **435**, 308 (2005).
- K. Shiroguchi and K. Kinoshita, Jr., *Science* **316**, 1208 (2007).
- R. D. Vale and R. A. Milligan, *Science* **288**, 88 (2000).
- C. Bustamante, Y. R. Chemla, N. R. Forde, and D. Izhaky, *Annu. Rev. Biochem.* **73**, 705 (2004).
- A. B. Kolomeisky and M. E. Fisher, *Annu. Rev. Phys. Chem.* **58**, 675 (2007).
- H. C. Berg, *E. coli in Motion* (Springer, New York, 2003).
- H. Noji, R. Yasuda, M. Yoshida, and K. Kinoshita, *Nature (London)* **386**, 299 (1997).
- T. Elston, H. Wang, and G. Oster, *Nature (London)* **391**, 510 (1998).
- H. Wang and G. Oster, *Nature (London)* **396**, 279 (1998).
- J. E. Molloy and C. Veigel, *Science* **300**, 2045 (2003).
- M. S. Liu, B. D. Todd, and R. J. Sadus, *J. Chem. Phys.* **118**, 9890 (2003).
- M. Karplus and Y. Q. Gao, *Curr. Opin. Struct. Biol.* **14**, 250 (2004).
- A. Yildiz, *Science* **311**, 792 (2006).
- R. J. Sadus, *Mol. Simul.* **34**, 23 (2008).
- E. R. Kay, D. A. Leigh, and F. Zerbetto, *Angew. Chem., Int. Ed.* **46**, 72 (2007).
- G. S. Kottas, L. I. Clarke, D. Horinek, and J. Michl, *Chem. Rev. (Washington, D.C.)* **105**, 1281 (2005).
- K. Kinoshita and T. Aida, *Chem. Rev. (Washington, D.C.)* **105**, 1377 (2005).
- W. F. Paxton, S. Sundararajan, T. E. Mallouk, and A. Sen, *Angew. Chem., Int. Ed.* **45**, 5420 (2006).
- W. R. Browne and B. L. Feringa, *Nat. Nanotechnol.* **1**, 25 (2006).
- R. Dreyfus, J. Baudry, M. L. Roper, M. Fermigier, H. A. Stone, and J. Bibette, *Nature (London)* **437**, 862 (2005).
- E. Gauger and H. Stark, *Phys. Rev. E* **74**, 021907 (2006).
- A. Najafi and R. Golestanian, *Phys. Rev. E* **69**, 062901 (2004).
- A. Najafi and R. Golestanian, *J. Phys.: Condens. Matter* **17**, S1203 (2005).
- R. F. Ismagilov, A. Schwartz, N. Bowden, and G. M. Whitesides, *Angew. Chem., Int. Ed.* **41**, 652 (2002).
- W. F. Paxton, K. C. Kistler, C. C. Olmeda, A. Sen, S. K. St. Angelo, Y. Cao, T. E. Mallouk, P. E. Lammert, and V. H. Crespi, *J. Am. Chem. Soc.*

- 126**, 13424 (2004).
- <sup>30</sup> S. Fournier-Bidoz, A. C. Arsenault, I. Manners, and G. A. Ozin, *Chem. Commun. (Cambridge)* **441** (2005).
- <sup>31</sup> W. F. Paxton, A. Sen, and T. E. Mallouk, *Chem.-Eur. J.* **11**, 6462 (2005).
- <sup>32</sup> G. A. Ozin, I. Manners, S. Fournier-Bidoz, and A. C. Arsenault, *Adv. Mater. (Weinheim, Ger.)* **17**, 3011 (2005).
- <sup>33</sup> T. R. Kline, W. F. Paxton, T. E. Mallouk, and A. Sen, *Angew. Chem., Int. Ed.* **44**, 744 (2005).
- <sup>34</sup> P. Dhar, T. M. Fischer, Y. Wang, T. E. Mallouk, W. F. Paxton, and A. Sen, *Nano Lett.* **6**, 66 (2006).
- <sup>35</sup> Y. Wang, R. M. Hernandez, D. J. Bartlett, J. M. Bingham, T. R. Kline, A. Sen, and T. E. Mallouk, *Langmuir* **22**, 10451 (2006).
- <sup>36</sup> L. Qin, M. J. Banholzer, X. Xu, L. Huang, and C. A. Mirkin, *J. Am. Chem. Soc.* **129**, 14870 (2007).
- <sup>37</sup> N. I. Kovtyukhova, *J. Phys. Chem. C* **112**, 6049 (2008).
- <sup>38</sup> R. Golestanian, T. B. Liverpool, and A. Ajdari, *Phys. Rev. Lett.* **94**, 220801 (2005).
- <sup>39</sup> J. R. Howse, R. A. L. Jones, A. J. Ryan, T. Gough, R. Vafabakhsh, and R. Golestanian, *Phys. Rev. Lett.* **99**, 048102 (2007).
- <sup>40</sup> D. J. Earl, C. M. Pooley, J. F. Ryder, I. Bredberg, and J. M. Yeomans, *J. Chem. Phys.* **126**, 064703 (2007).
- <sup>41</sup> G. Rückner and R. Kapral, *Phys. Rev. Lett.* **98**, 150603 (2007).
- <sup>42</sup> Y.-G. Tao and R. Kapral, *J. Chem. Phys.* **128**, 164518 (2008).
- <sup>43</sup> Y.-G. Tao and R. Kapral, *ChemPhysChem* **10**, 770 (2009).
- <sup>44</sup> A. Malevanets and R. Kapral, *J. Chem. Phys.* **110**, 8605 (1999).
- <sup>45</sup> A. Malevanets and R. Kapral, *J. Chem. Phys.* **112**, 7260 (2000).
- <sup>46</sup> A. Malevanets and R. Kapral, *Lect. Notes Phys.* **640**, 116 (2004).
- <sup>47</sup> K. Vissche, M. J. Schnitzer, and S. M. Block, *Nature (London)* **400**, 184 (1999).
- <sup>48</sup> K. Tucci and R. Kapral, *J. Chem. Phys.* **120**, 8262 (2004).
- <sup>49</sup> R. Kapral, *Adv. Chem. Phys.* **48**, 71 (1981).
- <sup>50</sup> R. Kapral, *Adv. Chem. Phys.* **140**, 89 (2008).
- <sup>51</sup> G. Gompper, T. Ihle, D. M. Kroll, and R. G. Winkler, *Adv. Polym. Sci.* **221**, 1 (2009).
- <sup>52</sup> D. Frenkel and B. Smit, *Understanding Molecular Simulation—From Algorithms to Applications* (Academic, San Diego, 1996).
- <sup>53</sup> T. Ihle and D. M. Kroll, *Phys. Rev. E* **63**, 020201 (2001).
- <sup>54</sup> T. Ihle and D. M. Kroll, *Phys. Rev. E* **67**, 066705 (2003).
- <sup>55</sup> Y.-G. Tao, I. O. Götzke, and G. Gompper, *J. Chem. Phys.* **128**, 144902 (2008).
- <sup>56</sup> N. Kikuchi, C. M. Pooley, J. F. Ryder, and J. M. Yeomans, *J. Chem. Phys.* **119**, 6388 (2003).
- <sup>57</sup> M. Ripoll, R. G. Mussawisade, K. Winkler, and G. Gompper, *Phys. Rev. E* **72**, 016701 (2005).
- <sup>58</sup> F. Jülicher, A. Ajdari, and J. Prost, *Rev. Mod. Phys.* **69**, 1269 (1997).
- <sup>59</sup> H. Wang and G. Oster, *Europhys. Lett.* **57**, 134 (2002).
- <sup>60</sup> J. T. Finer, R. M. Simmons, and J. A. Spudich, *Nature (London)* **368**, 113 (1994).
- <sup>61</sup> D. E. Smith, S. J. Tans, S. B. Smith, S. Grimes, D. L. Anderson, and C. Bustamante, *Nature (London)* **413**, 748 (2001).